

Available online at www.sciencedirect.com



journal homepage: www.elsevier.com/locate/jmrt



Original Article

Effect of Zr addition on the local structure and mechanical properties of Ti—Ta—Nb—Zr refractory high-entropy alloys



Guangyun Ji a,1, Zhukun Zhou b,c,1, Fanchao Meng a,1, Xiao Yang a,1, Ruixin Sheng a,1, Jingbo Qiao a,1, Peter K. Liaw a,1, Mo Li a,1, Liang Jiang a,1, Shuying Chen a,1, Yang Tong a,1

- ^a Institute for Advanced Studies in Precision Materials, Yantai University, Yantai, Shandong 264005, China
- ^b School of Materials Science and Engineering, Georgia Institute of Technology, Atlanta, GA 30332, USA
- ^c School of Mechanical Engineering, Guangxi University, Nanning, Guangxi 530004, China
- ^d Key Laboratory of Cryogenics, Technical Institute of Physics and Chemistry, Chinese Academy of Sciences, Beijing 100190, China
- ^e Department of Materials Science and Engineering, The University of Tennessee, Knoxville, TN 37996, USA

ARTICLE INFO

Article history: Received 19 May 2022 Accepted 29 June 2022 Available online 6 July 2022

Keywords:
Refractory high-entropy alloy
Microstructure
Local lattice distortion
Solid-solution strengthening
First-principles calculations

ABSTRACT

Solid solution strengthening is the major strengthening mechanism that accounts for the high strength of single-phase body-centered cubic (BCC) refractory high-entropy alloys (RHEAs). Local lattice distortion (LLD), often regarded as one of the core effects of HEAs, is generally believed to be deterministic in solid solution strengthening for RHEAs since the loosely packed BCC crystal structure can accommodate significant LLD. To systematically investigate the effect of LLD on solid solution strengthening, the present study deliberately introduced different degrees of LLD in the experimentally fabricated BCC Ti_{65-x}Ta₂₅Nb₁₀Zr_x (x = 0, 5, 10, 15, and 20) RHEAs by varying the Zr content. Subsequently, by combining experimental analysis, first-principles calculations, and theoretical modeling, it is found that yield strength, hardness, atomic radii, and LLD increase with the increase of Zr content. Moreover, through quantitative solid-solution strengthening analysis, it is demonstrated that the modulus mismatch dominates solid solution strengthening over LLD even for severely distorted Zr-containing RHEAs, contrary to the generally accepted assumption that solid solution strengthening is mainly from LLD effect. What's even more surprising is that the increase of Zr content accelerates grain growth, opposite to the sluggish diffusion effect proposed for HEAs. Our results shall guide the elemental selection for the design of high-strength RHEAs eradicating the random sampling in the endless compositional pool. © 2022 The Author(s). Published by Elsevier B.V. This is an open access article under the CC BY-NC-ND license (http://creativecommons.org/licenses/by-nc-nd/4.0/).

^{*} Corresponding author.

^{**} Corresponding author.

E-mail addresses: sychen@ytu.edu.cn (S. Chen), yt1@ytu.edu.cn (Y. Tong).

¹ These authors contributed equally to this work.

1. Introduction

High-entropy alloys (HEAs), metallic solid solutions composed of multiple components at equiatomic or near-equiatomic concentration, provide a new alloy design strategy [1–4]. The compositional complexity stemmed from the differences of atomic sizes and chemistry makes HEAs possess diversified local atomic configurations [5,6]. In particular, the compositional complexity generates the atomic-level distortion even though the average lattice of HEAs remains undistorted as pure metals do [7,8]. The local lattice distortion (LLD), considered as one of the core effects for HEAs, have been exploited for the advanced alloy design to achieve both high strength and excellent radiation performance [9–13].

The extent of LLD in HEAs varies from one composition to another, which has been examined by both simulations and experiments [14–17]. Through synchrotron X-ray total scattering technique, the LLD in face centered-cubic (FCC) HEAs including CoCrFeNi, CoCrFeMnNi, and CoCrFeNiPd has been quantitatively measured [14]. The LLD in the FCC HEAs composed of only 3d transition metals is relatively small, which cannot provide a static defect pinning effect for radiation applications because a surge of lattice expansion relaxes the LLD at even low radiation doses [11]. However, no relaxation phenomenon was observed for the CoCrFeNiPd HEA with a relatively large LLD [15], suggesting that a critical LLD value is required for an effective suppression of radiationdefect growth. The crystal structure is another important factor for the extent of LLD. After characterizing the crystal structure of 2478 HEAs, Kube et al. [18] found that HEAs with large atomic-size mismatch preferentially forms body centered-cubic (BCC) structure rather than FCC. Seemingly, the loosely packed BCC structure has more free space to accommodate the large LLD. Indeed, the synchrotron X-ray study of the local structure of 15 BCC HEAs reveals that the Zr and/or Hf-containing refractory HEAs (RHEAs) break down the 15% atomic-size difference in Hume-Rothery rules by exhibiting severe LLD [19]. The density functional theory (DFT) calculation demonstrates that the mean square atomic displacement in HfNbTiZr even meets the Lindemann melting criterion [20]. These findings seemingly reveal a clear path for the design of high-performance alloys through tuning the atomic-level distortions by the proper element selection.

Due to the difference in atomic size and shear modulus among different principal elements, noticeable local heterogeneity is produced in HEAs. Tuning local heterogeneity of atomic sizes and shear modulus provides a way to design strong HEAs. Lee et al. recently reported that the addition of large atom Zr into BCC NbTaTiV HEA increases its yield strength by ~300 MPa [21]. Sohn et al. found that the FCC VCoNi medium-entropy alloy (MEA) with the largest LLD has the highest yield strength when compared with CrCoNi MEA and CrMnFeCoNi HEAs with similar grain sizes [22]. By DFT calculations, Oh et al. found that, rather than LLD, electronegativity difference is the dominant factor for the high yield strength in NiV FCC concentrated solid solution alloys [23]. Although experimental studies claim that the LLD is an effective way to increase the yield strength of HEAs, a

quantitative examination of the influence of LLD on mechanical performance is still missing. The objective of this study is to quantitatively verify the LLD contribution to the solid solution strengthening in BCC HEAs.

In the present study, we chose the Ti—Ta—Nb system as the base and then examined the effect of adding large Zr atoms into the base alloy on the LLD and mechanical properties. One consideration for the choice of Ti, Ta, and Nb elements is their similar atomic sizes so that the LLD effect induced by the introduction of Zr can be clarified. Also, a density comparable to the Ni-based superalloys (~8 g/cm³) is one constraint to optimize the composition. By integrating different simulation and characterization tools, we systematically examined the microstructure, local structure and mechanical properties of the Ti—Ta—Ni—Zr RHEAs. The contributions of both the atomic-size difference and modulus mismatch to solid-solution strengthening are discussed for the designed HEAs with large LLD.

2. Methodology

2.1. DFT modeling

DFT calculations were carried out employing the Vienna Ab initio Simulation Package (VASP) code with the projector augmented wave approach [24,25]. The input structure with 250 atoms was constructed by the special quasi-random structures (SQS) model to ensure the random arrangement of different types of atoms at the first and second-nearest neighbor sites [26]. All of the SQS structure was generated in the ICET package [27]). The Perdew-Burke-Ernzerhof (PBE) gradient approximation was chosen for the exchangecorrelation functional. The orbital electrons were considered for metal elements with 4, 12, 11, and 5 electrons used for Ti $(3d^34s^1)$, Zr $(4s^24p^65s^24 d^2)$, Nb $(4p^65s^14 d^4)$ and Ta $(6s^25 d^3)$, respectively. Brillouin-zone integrations were performed, using a 2 \times 2 \times 2 k-point mesh in the scheme of Monkhorst-Pack (MP). The plane-wave energy cutoff was 300 eV, and the force convergence criterion was set to 0.02 eV/ A. In the DFT calculations, volume relaxation only was conducted first and then fully-relaxed structure was obtained by allowing the changes of both ion positions and volume. The elastic constants were calculated by fitting the polynomial function of the strain-energy curves [28]. There are three independent elastic constants in BCC structure. So the applied strains in this work are $\eta_A = [\varepsilon, 0, 0, 0, 0, 0]$, $\eta_B = [\varepsilon, \varepsilon, 0, 0, 0, 0]$, $\eta_C = [0, 0, 0, 2\varepsilon, 0, 0]$. All of the DFT calculations were performed at zero temperature.

2.2. Experimental procedure

RHEAs with the nominal compositions of $Ti_{65-x}Ta_{25}Nb_{10}Zr_x$ (x = 0, 5, 10, 15, and 20), denoted as TTNZ alloys below, were prepared by arc melting Ti, Ta, Nb and Zr metals (purity >99.95%) under an argon atmosphere. Alloy ingots were remelted at least five times to ensure homogeneity. The solidified buttons were cut into slabs with dimensions of 11 mm \times 20 mm \times 45 mm. Cold rolling was then conducted

with a thickness reduction of 70%. The rolled sheets were sealed in vacuum-quartz tubes and then heat treated at $1100 \, ^{\circ}$ C for 5 min, followed by water quenching.

After the heat treatment, the phase identification was performed by X-ray diffraction (XRD) of Shimadzu 7000 X, using Cu K α radiation on carefully ground specimens with SiC paper. The measurement were conducted through 20 scan ranging from 30 to 90° with a scan rate of 5°/min. A scanning electron microscope of Zeiss Sigma 300 (SEM) equipped with electron-backscatter diffraction (EBSD) and energy disperse spectroscopy (EDS) were utilized for the microstructure and composition analysis.

Samples with a geometry of 3 mm \times 3 mm \times 5 mm were machined and polished for compression experiments. Compression tests with a strain rate of $10^{-3}~\text{s}^{-1}$ were performed at room temperature using an INSTRON 8801 testing machine under the displacement-control mode. Hardness of TTNZ alloys was measured by a Vickers hardness tester (HuaYin Hv-1000A) with the load of 300 g and a dwell time of 10 s.

3. Results

3.1. Microstructure

Fig. 1 presents the XRD profiles of TTNZ alloys. Through indexing the XRD peaks, we found that all alloys have the simple BCC crystal structure. Their lattice constants were obtained by fitting the full profile in the GSAS software [29]. Table 1 lists the lattice constant values. It can be seen that the lattice constant increases with the Zr concentration since the atomic size of Zr is larger than those of Ta, Nb, and Ti. Thus, the large lattice space is needed to accommodate the large Zr atoms in the studied alloys [30]. DFT calculations were further performed to obtain the lattice constants at zero temperature. The lattice constants calculated from the DFT at zero temperature are marginally smaller than the experimental values

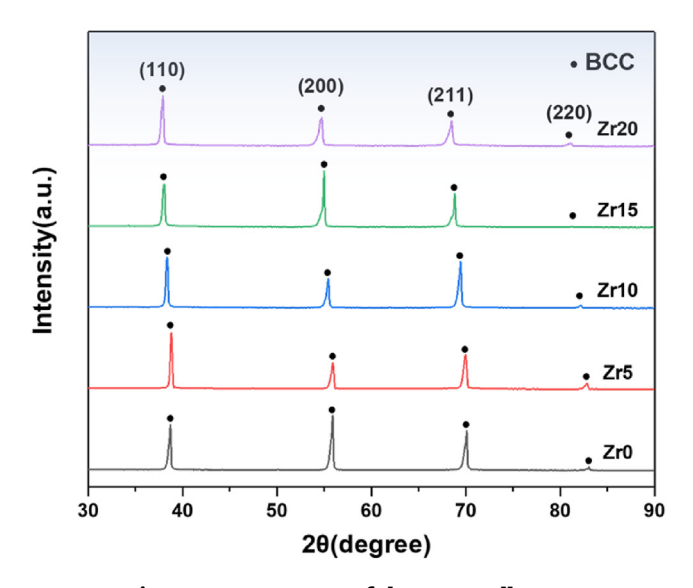


Fig. 1 - XRD pattern of the TTNZ alloys.

Table 1 - A comparison of experimental lattice constants and ones calculated through DFT.

Alloy	a _{exp} (Å)	a _{DFT} (Å)
Zr0	3.287	3.263
Zr5	3.290	3.284
Zr10	3.314	3.301
Zr15	3.350	3.338
Zr20	3.355	3.346

measured at room temperature, indicating reasonable agreement between the DFT calculations and measurements with the consideration of thermal expansion effect.

Fig. 2 shows the inverse pole figures (IPFs) of TTNZ RHEAs. The IPF results reveal that the cold-rolled samples are fully recrystallized without apparent preferred orientation after the heat treatment at 1100 °C. The grain sizes of these recrystallized samples were statistically determined as 22.8 μm for Zr0, 24.8 μm for Zr5, 32.1 μm for Zr10, 37.7 μm for Zr15, and 43.5 μm for Zr20. Compared with the Zr0 sample, the grain size of the Zr20 sample increase by ~50%. The grain growth is significantly enhanced by the addition of large Zr atoms, indicating fast atomic diffusion in TTNZ RHEAs. Additionally, the compositional homogeneity of the TTNZ RHEAs was examined by SEM-EDX. No obvious chemical segregation was found in these samples. Table 2 lists the experimental compositions of each sample. The experimental content of each individual element is highly close to the nominal composition.

3.2. Local structure

In the above XRD study, the average crystal structure generates Bragg diffraction peaks as pure metals do, but the local structure in HEAs is no longer perfect. Here, DFT calculations were conducted to examine the local structure of the TTNZ alloys. Note that supercells with random atomic arrangements were utilized as the initial structure in the DFT calculations. The fully-relaxed supercells of TTNZ alloys are shown in Fig. 3. Clearly, atoms distort locally from their ideal lattice positions in each alloy although their crystal structure remains BCC on average. However, the magnitude of LLD seemingly becomes pronounced with the addition of Zr concentration, which is expected from the large atomic size difference between Zr and other three atomic species.

A commonly-used parameter to quantize the LLD in HEAs is the atomic size mismatch [31]:

$$\delta = \sqrt{\sum_{i=1}^{N} c_i \left(1 - r_i / \sum_{j=1}^{N} c_j r_j\right)^2}$$
 (1)

where N is the number of atomic species, and $c_{i,j}$ and $r_{i,j}$ are molar concentration and atomic radius of the ith or jth element, respectively. To calculate the δ values of TTNZ alloys, the atomic radius was firstly determined for each atom in the fully relaxed supercell by the Voronoi tessellation method, as shown in Fig. 4a—e. It can be seen that the radius values of each atomic specie fluctuate, revealing the diversity of local atomic environments in HEAs. Meanwhile, the addition of Zr enhances the fluctuation of atomic radius for other three

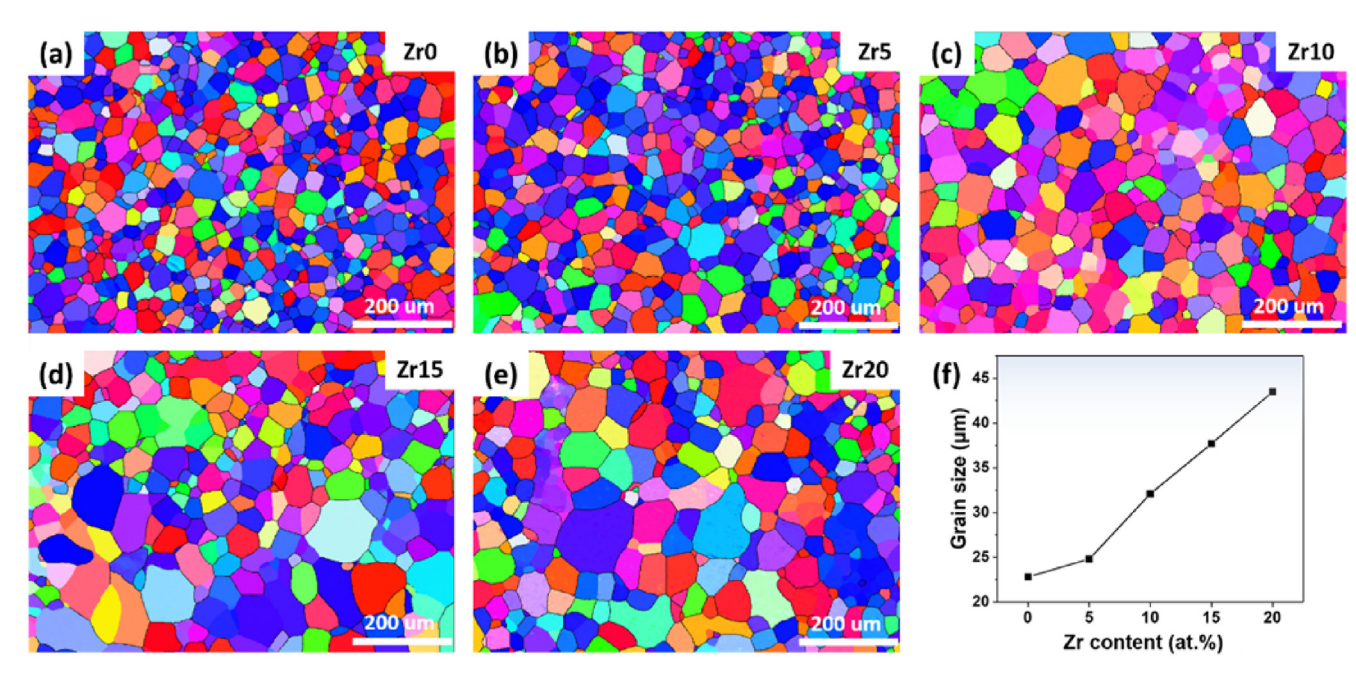


Fig. 2 - (a-e) IPF and (f) average grain size of the TTNZ alloys after heat-treated at 1100 °C for 5 min.

elements. Based on the average atomic radius value of each element, the atomic size mismatch was calculated as 0.08%, 0.63%, 0.89%, 1.05%, and 1.13% for Zr0, Zr5, Zr10, Zr15, and Zr20, respectively. In the calculation of atomic size mismatch in HEAs, a hard sphere approach has been often adopted by assuming a negligible charge transfer effect among constituent elements in alloys. The atomic radius value for every atomic specie is fixed in the hard sphere model. Here, we calculated δ based on the atomic Wigner-Seitz (WS) radii, r_{ws} , of BCC Ti, Ta, Nb and Zr pure metals. The WS radii were calculated from the experimental lattice constant of pure metals by $4/3\pi^*r_{ws}^2=a^3/2$. From the hard sphere model, the atomic size mismatch was calculated as 0%, 1.9%, 2.6%, 3.12%, and 3.48% for Zr0, Zr5, Zr10, Zr15, and Zr20, respectively. Comparing with the DFT calculations, the hard sphere approach significantly overestimates the atomic size mismatch for the Zr-containing TTNZ alloys. The underlying reasons are twofold. First, the electronegativity difference among constituent elements causes the charge transfer from larger Zr atoms to smaller Ti, Ta and Nb atoms to reduce the

atomic size mismatch, as demonstrated in previous DFT studies [19]. Second, the supercell volume expands to accommodate the large Zr atoms, as revealed by the radius increase of each atomic specie in Fig. 4f. The average atomic radius difference is reduced profoundly by these two effects, but the fluctuation of atomic radius can be dramatic even for the Zr0 alloy with a negligible difference of average atomic radius among constituent elements. These results are consistent with our previous finding that severe LLD exists in the Zr-containing RHEAS [19,32].

3.3. Elastic properties

Elastic anisotropy is known to impact various mechanical performance of alloys, such as phase transformation, dislocation dynamics and crack propagation. Hence the elastic anisotropy has been a property of interest for the mechanical property prediction of HEAs. Since the DFT calculations have been successfully applied for the predication of elastic properties of BCC HEAs, the composition dependence of elastic

Table 2 $-$ Compositions of the TTNZ alloys.							
Alloy		Ti	Ta	Nb	Zr		
Zr0	Nominal	65	25	10	0		
	Experimental	65.0 ± 0.4	25.6 ± 0.5	9.4 ± 0.1	0		
Zr5	Nominal	60	25	10	5		
	Experimental	61.4 ± 0.9	26.7 ± 1.1	8.3 ± 0.1	3.6 ± 0.4		
Zr10	Nominal	55	25	10	10		
	Experimental	55.7 ± 1.1	25.4 ± 1.4	9.5 ± 0.2	9.4 ± 0.5		
Zr15	Nominal	50	25	10	15		
	Experimental	55.0 ± 0.3	23.9 ± 1.1	8.5 ± 0.1	12.6 ± 0.9		
Zr20	Nominal	45	25	10	20		
	Experimental	45.9 ± 0.6	24.8 ± 0.8	10.2 ± 0.4	19.1 ± 0.7		

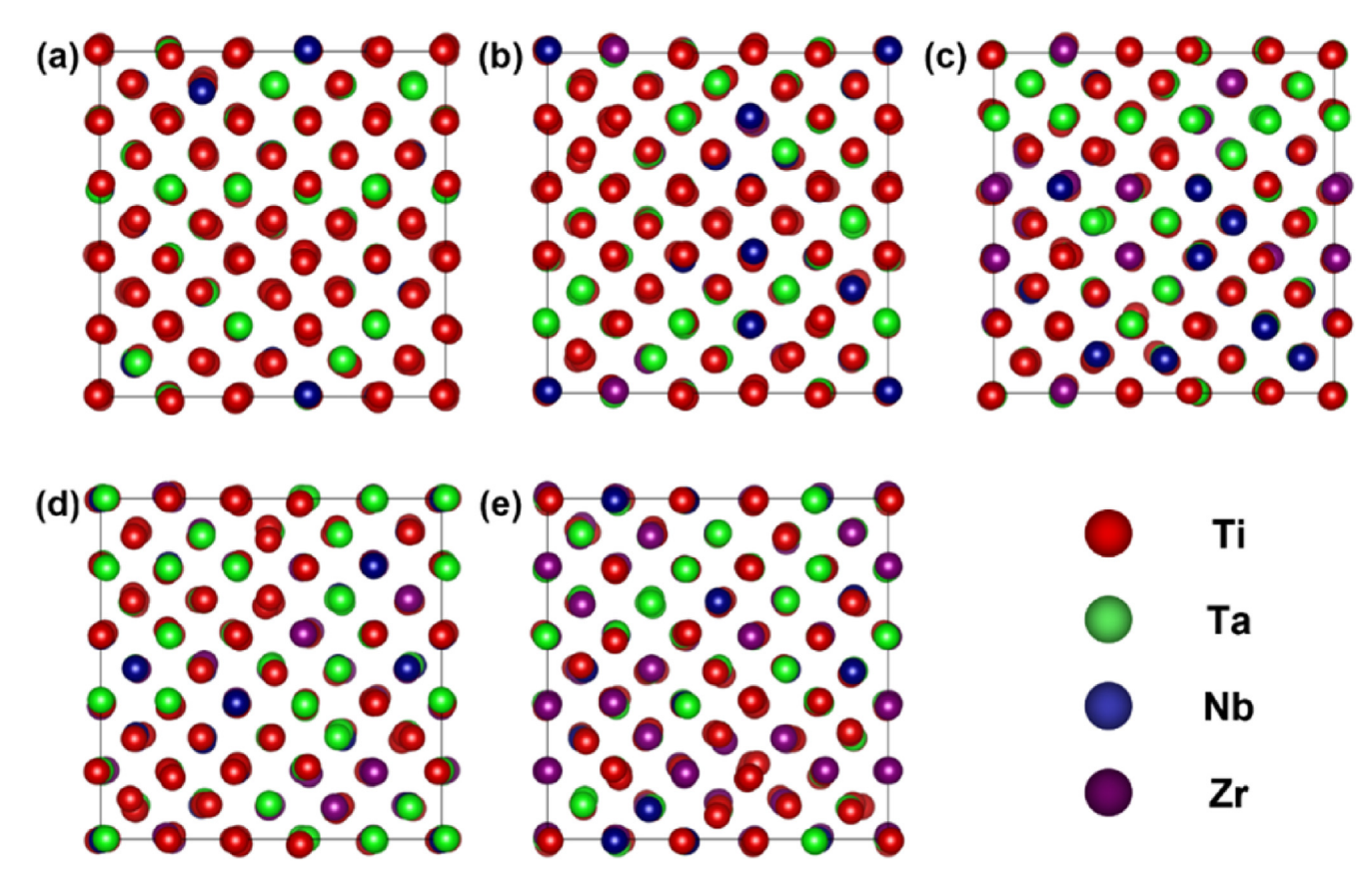


Fig. 3 — A projection view of the fully-relaxed supercells for (a) Zr0, (b) Zr5, (c) Zr10, (d) Zr15 and (e) Zr20 HEAs along the [001] axis.

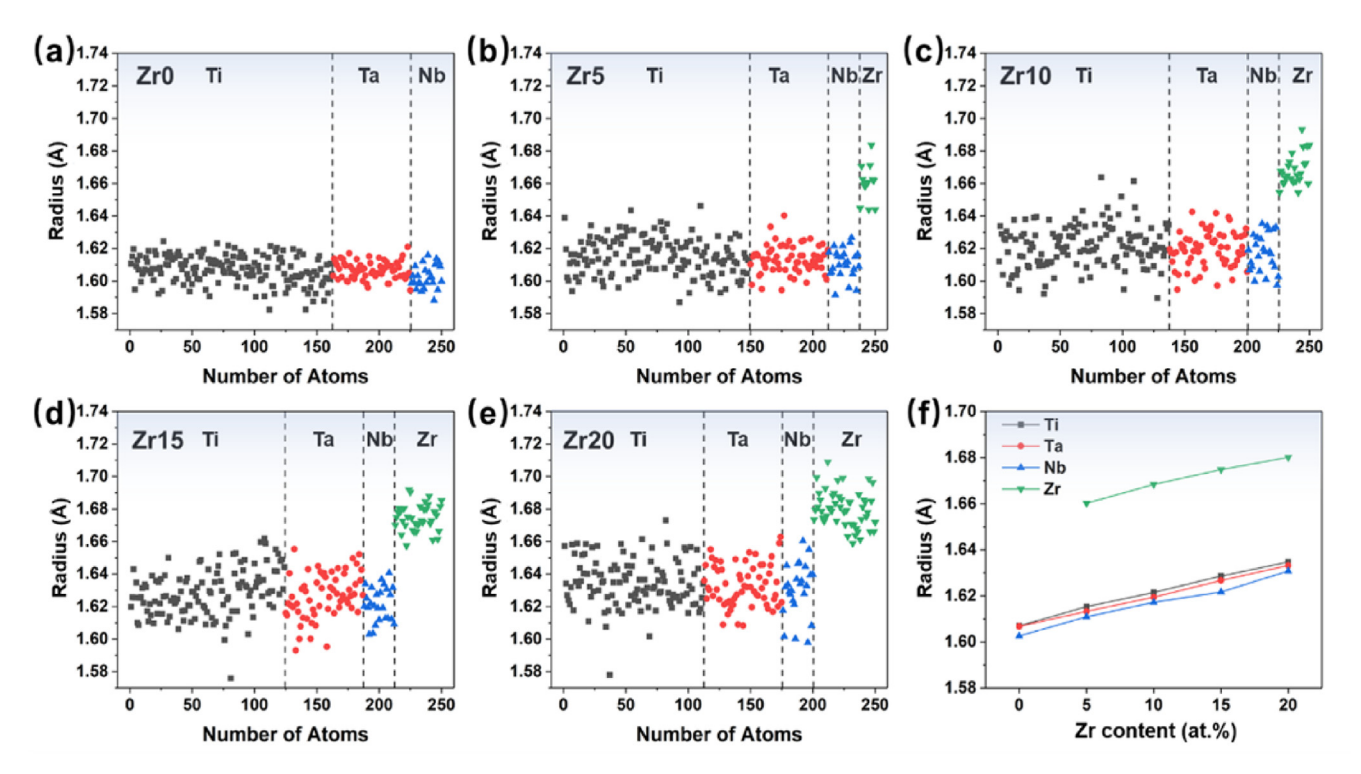


Fig. 4 - (a-e) Species-resolved atomic radius for TTNZ alloys obtained from the DFT calculations; (f) average radius for each species in the TTNZ alloys.

Table 3 — Elastic moduli calculated using DFT.								
Alloy	C ₁₁ (GPa)	C ₁₂ (GPa)	C ₄₄ (GPa)	A_z	B (GPa)	E (GPa)	G (GPa)	N
Zr0	162	130	36	2.19	141	73	26	0.41
Zr5	161	117	34	1.55	131	80	29	0.4
Zr10	155	117	37	1.92	129	79	28	0.4
Zr15	159	109	39	1.56	126	89	32	0.38
Zr20	151	110	37	1.82	124	81	29	0.39

properties of TTNZ alloys is also examined by DFT. First, the single-crystal elastic constants, C_{ij} , for each TTNZ alloy were obtained by fitting the strain-energy curves. Based on the calculated C_{ij} , the Zener anisotropy factor, $A_z = 2C_{44}/(C_{11} - C_{12})$, was then derived, as listed in Table 3. Compared with the parent Zr0 alloy, the addition of Zr content decreases A_z . The A_z values of Zr5 and Zr15 alloys are close to that of the isotropic state, 1, representing less dependence of the elastic response on the loading direction. To further visualize the anisotropy of elastic properties, the directional dependence of Young's modulus, E_z , and shear modulus, E_z , are plotted in Fig. 5. Here, the elastic properties in an arbitrary crystallographic orientation are calculated through the following equations [33,34]:

$$\frac{1}{E} = S_{11} - 2\left(S_{11} - S_{12} - \frac{S_{44}}{2}\right) \left(l_1^2 l_2^2 + l_2^2 l_3^2 + l_3^2 l_1^2\right) \tag{2}$$

$$\frac{1}{G} = S_{44} + 4(S_{11} - S_{12} - S_{44} / 2) \left(l_1^2 l_2^2 + l_2^2 l_3^2 + l_3^2 l_1^2 \right) \tag{3}$$

where $S_{11}=(C_{11}+C_{12})/[(C_{11}-C_{12})/(C_{11}+2C_{12})]$, $S_{12}=-C_{12}/[(C_{11}-C_{12})/(C_{11}+2C_{12})]$ and $S_{44}=1/C_{44}$ are elastic compliances, and l_i is the direction cosines. From Fig. 5, it can be seen that the highest value of E is along the <111> directions while the lowest value along the <100> ones. However, G shows a completely opposite trend of E.

From the single-crystal elastic constants, the moduli of polycrystalline TTNZ alloys were calculated based on the Voigt-Reuss-Hill approach [35]. Table 3 indicates that the

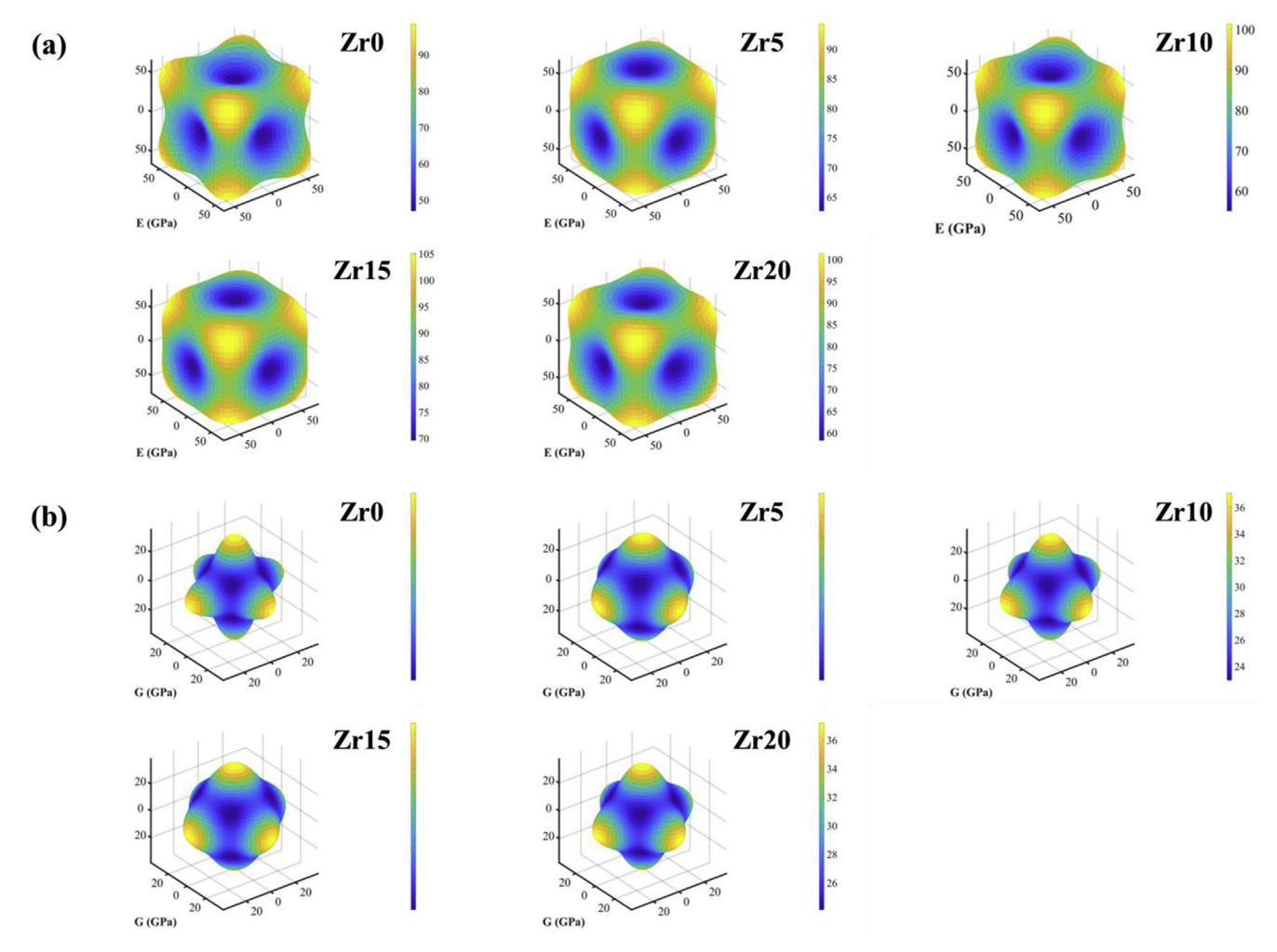


Fig. 5 – Directional dependence of Young's modulus (a) and shear modulus (b) for TTNZ alloys. The X, Y and Z axes represent [100], [010] and [001], respectively.

polycrystalline bulk modulus, B, decreases with the addition of Zr, but E, G and ν show no clear compositional dependence. These average elastic properties show less compositional dependence, but the elastic modulus mismatch in local areas can fluctuate significantly due to diversified local atomic configurations as discussed later.

The ductile behavior of BCC HEAs can be empirically predicted by the Pugh ratio (B/G). Here, B reflects the resistance against cleavage while G reveals the difficulty of dislocation movement. From the brittle-to-ductile criterion of the Pugh ratio (B/G), the transition limit is equivalent to $\nu > 0.26$. The Poisson's ratio values of TTNZ alloys are much higher than this empirical criterion, suggesting that these TTNZ alloys are ductile, as demonstrated by mechanical testing results below.

3.4. Compressive properties

Fig. 6 shows compressive engineering stress-strain curves of the TTNZ alloys. It is apparent that with the increase of Zr content, the yield strength of alloys was improved gradually from 452 MPa to 934 MPa. Yield strength values are list in Table 4. Compared with the Zr-free sample, the σ_y of Zr20 alloy was increased by ~100%. Meanwhile, TTNZ alloy exhibits excellent plasticity, indicating an outstanding malleability. Note that compression tests were not continued after samples have no clear evidence of fracture. These experimental findings are consistent with the predictions based on elastic property calculations.

4. Discussion

4.1. Zr effect on grain growth

Although average grain size increases monotonically with the increasing concentration of Zr, abnormal grain growth was found in Zr15 and 20 alloys with a coexistence of a number of finer grains and a limited number of anomalously large grains.

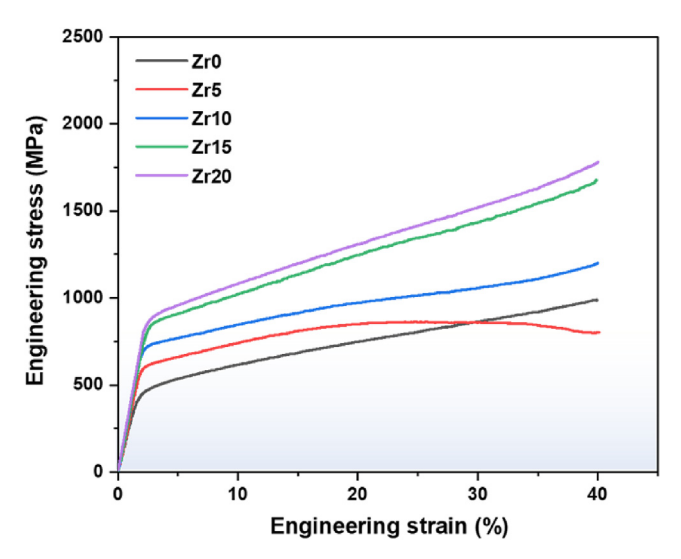


Fig. 6 - Compressive engineering stress-strain curves of TTNZ alloys.

Table 4 $-$ The specific values of yield strength in TTNZ alloys.								
Alloy	Zr0	Zr5	Zr10	Zr15	Zr20			
σ _y (MPa)	452.2	617.4	729.7	884.4	934			

Our experimental results reveal that grain growth rate of the Zr-free HEA is lower than the Zr20 alloy, different from other studies that the Zr addition in (CrTaNbMoV) Zrx HEAs delays the grain growth [36]. The grain growth process in singlephase alloys involves kinetic processes of grain-boundary migration, which is correlated with the cooperative diffusion of constituent elements. It is reported that the atomic diffusion is strongly dependent on the temperature, composition, and crystal structure [37]. In present study, five alloys with bcc structure were annealed simultaneously at 1100 °C excluding the effect of temperature and structure. Thus, the diffusion activity in TTNZ RHEAs should be determined by the composition variation. As displayed in Fig. 2, Zr element has significant effect on accelerating the grain growth during annealing process. Cao and Bai et al. [38,39] presented that the Zr has the largest diffusion coefficient among these four components of Ti, Zr, Ta, and Nb. Wang et al. [40,41] studied the diffusion behavior in Zr-Nb, Zr-Ta binary and Zr-Nb-Ta ternary system and found the Zr addition enhanced the diffusion of Ta and Nb element. In another study of Ti-Al-Zr system, Zr was found to promote the diffusion of Ti element [42]. It is known that grain boundary migration relies on the cooperative diffusion of all constituent atoms in order to avoid composition cleaving. It can be conceived that the cooperative accelerated diffusion of different elements in the TTNZ RHEAs accelerates the rate of boundary movement and thus the grain growth. The addition of Zr reduces the sluggish diffusion effect, one of four core effects in HEAs. Moreover, previous study [43] demonstrated that an increase of the solute content in alloys increases the diffusivity when accompanied by a decrease in the solidus temperatures. In the calculated phase diagram of TTNZ RHEAs (not shown), the solidus temperature indeed decreases with increasing Zr content, consistent with the enhanced diffusion event. Previous studies [44] reported that the severe LLD may reduce the grain growth by inhibiting diffusion of constituents, but it is not observed in the present study. Hence, it is implied that the rapid diffusion of Zr may exceed the effect of lattice distortion.

4.2. Zr effect on solid solution strengthening

The addition of Zr can efficiently increase the yield strength of ${\rm Ti}_{65}{\rm Ta}_{25}{\rm Nb}_{10}$ base alloy by ~28 MPa/at%, which is even larger than the previous NbTaTiV RHEA with the addition of 20% Zr leading to the enhancement of yield stress by ~300 MPa [21]. Notice that the LLD in the NbTaTiVZr HEA is much higher due to the large atomic size difference between smaller V and larger Zr. Apparently, alloying Zr has a significant impact on the achieved very high solid-solution strengthening. Compared with other three constituent elements in TTNZ alloys, the atomic radius of Zr is rather large to cause severe LLD as demonstrated by the DFT calculations mentioned

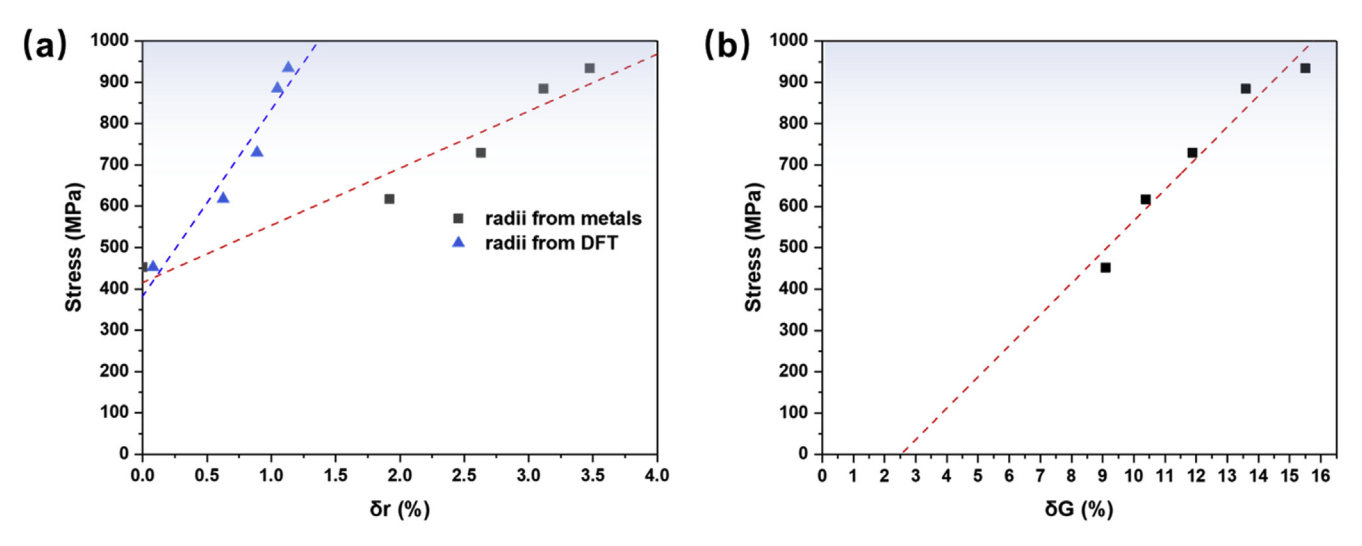


Fig. 7 — Correlation of yield strength with the LLD parameter, δ , (a) and modulus mismatch (b). For the δ calculations, the radius values of constituents from DFT and pure metals are both used.

above. It is expected that LLD is a key factor for the enhanced solid-solution strengthening. The correlation between yield strength and δ was shown in Fig. 7a. It can be seen that the yield strengths of TTNZ alloys have a positive linear correlation. However, it cannot be drawn a conclusion that LLD is the dominant contribution factor for the solid-solution strengthening since a similar positive linear relationship is also found between the yield strength and modulus mismatch. Here, the

modulus mismatch is calculated by
$$\delta_G = \frac{9}{8} \sum c_i \sum c_j \left| \frac{2(G_i - G_j)}{G_i + G_j} \right|$$
 [45],

where $c_{i,j}$ and $G_{i,j}$ are the concentration and shear modulus of ith or jth constituent element. Even though the shear modulus barely changes with the Zr concentration as examined by DFT calculations, the modulus mismatch is increased locally by the increase of composition complexity. To understand their effect on solid solution strengthening, the individual contribution of LLD and modulus mismatch should be evaluated quantitatively.

The yield strength in RHEAs can be estimated by

$$\sigma_{\rm v} \approx \sigma_{\rm mix} + \Delta \sigma$$
 (4)

here, σ_{mix} is the base strength estimated from the yield strength of a pure metal using the rule of mixture (ROM),

$$\sigma_{mix} = \sum c_i \sigma_{0.2(i)} \tag{5}$$

where c_i is the molar content of the i element, and $\sigma_{0.2(i)}$ is the yield strength of a pure metal, and $\Delta\sigma$ accounts for both grain boundary strengthening and solid-solution strengthening,

$$\Delta \sigma = \sigma_{qb} + \sigma_{ss} \tag{6}$$

$$\sigma_{qb} = kd^{-\frac{1}{2}} \tag{7}$$

$$\sigma_{ss} = \left(\sum A_{2}^{\frac{3}{2}} G_{2}^{\frac{3}{2}} c_{i} f_{i}^{2}\right)^{\frac{2}{3}}$$
 (8)

where k is a constant (240 MPa· μ m^{1/2}, adopted from the HfNbTaTiZr RHEA [46]), d is the average grain size, A = 0.04 [45] is a material-dependent dimensionless constant, $G = \sum c_i G_i$ is

the shear modulus of the alloy calculated based on ROM, and the parameter of f_i is given by the following expression [47]:

$$f_{\rm i} = \sqrt{\alpha^2 \delta_{\rm r_i}^2 + \delta_{\rm G_i}^2} \tag{9}$$

here, α is a constant determined by the type of mobile dislocations, and δ_{G_i} and δ_{r_i} are parameters addressing the atomic modulus and atomic-size mismatches, respectively. The α value is 2–4 for scrxew dislocations, and \geq 16 for edge dislocations [45]. Since a dislocation type in alloys is a random mixture of edge and screw dislocations, the value of α is specified as 9 [48]. In the BCC lattice, the atomic-size and elastic modulus mismatches in the vicinity of the i element can be evaluated as the average difference of the atomic size and modulus with its first nearest neighboring atoms, respectively:

$$\delta_{r_i} = \frac{9}{8} \sum_{j} c_j \frac{2(r_i - r_j)}{r_j + r_j} \tag{10}$$

$$\delta_{G_i} = \frac{9}{8} \sum_{i} c_j \frac{2(G_i - G_j)}{G_i + G_i}$$
(11)

Fig. 8a compares the experimental yield strength with the calculated yield strength from Eqs. 4–11. The atomic radius, shear modulus, and yield strength of pure metals are from Refs [49,50]. The calculations reasonably agree with the experimental results, and solid-solution strengthening, $\Delta \sigma$, plays a dominant factor on the hardness improvement in TTNZ alloys. Since the compression test is relatively sensitive to a variety of material defects, hardness test is also conducted to verify the accuracy of calculated yield strength. Studies [47,51] have demonstrated that the hardness in refractory HEAs follows the relationship with yield strength:

$$HV \approx 3\sigma_{\gamma} \tag{12}$$

Fig. 9 presents the Vickers hardness change with the Zr concentration for the TTNZ alloys. With the addition of Zr content, the hardness of these alloys monotonously increases

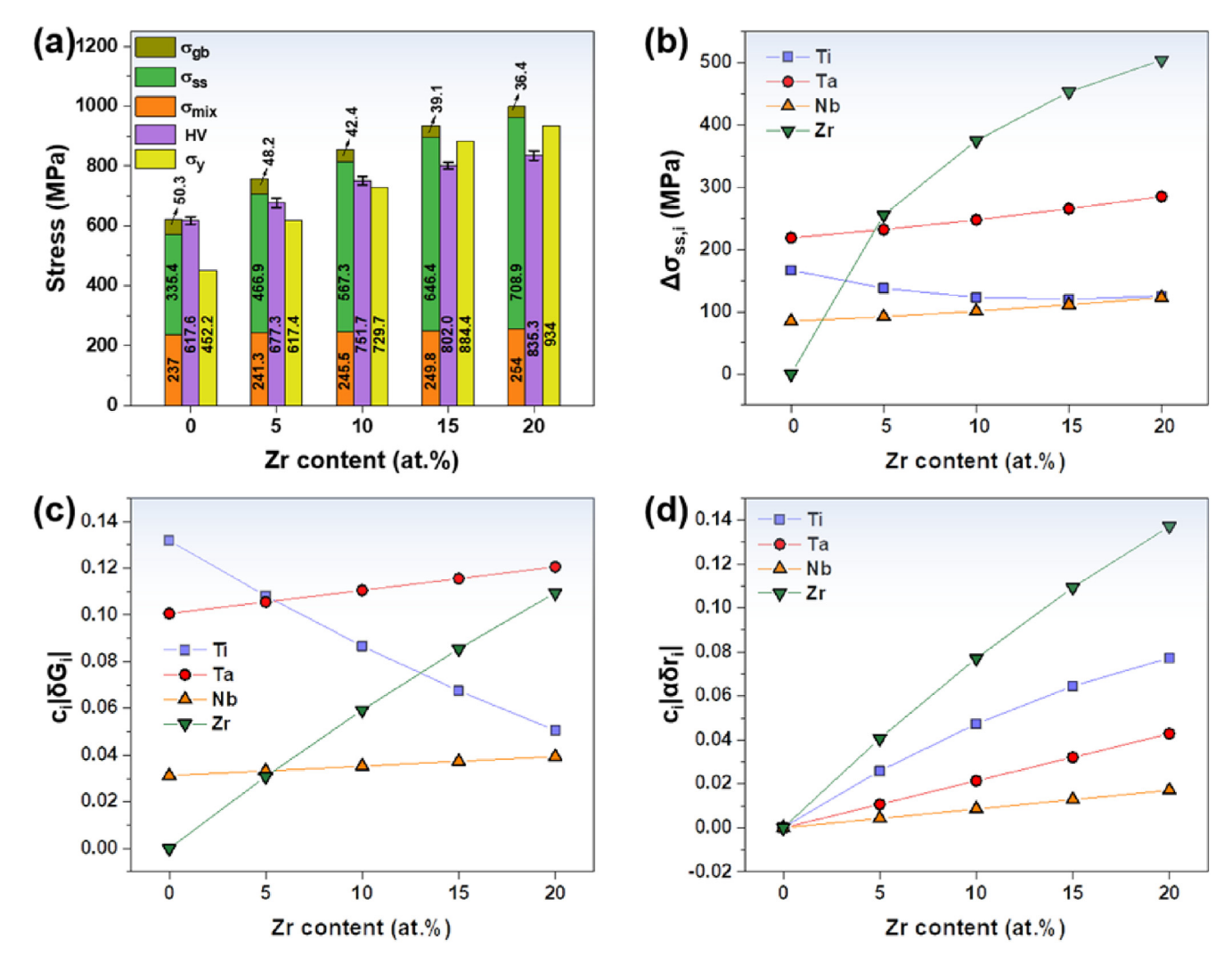


Fig. 8 - (a) A comparison of the predicted hardness and experimental hardness and compressive yield stress values. (b) Zr dependence of solid solution strengthening (b), shear modulus mismatch (c) and atomic size mismatch (d).

from 185 HV for the Zr0 alloy to 250 HV for the Zr20 alloy. The addition of 20 at.% Zr causes a remarkable hardness increase, ~35%. By comparing of the calculated yield strength and the yield strength obtained from hardness test in Fig. 8a, it is clearly seen that they match each other very well, indicating the reliable calculation from Eqs. 4–11.

The contribution of each element to the solid-solution strengthening was further evaluated, as shown in Fig. 8b. When the Zr concentration is higher than 5 at.%, the contribution pertaining to the Zr element outweighs contributions pertaining to other elements. Moreover, the addition of Zr enhances the contributions from the Ta and Nb-centered atomic environments although their concentrations are fixed in the TTNZ alloys, demonstrating the importance of a local chemistry change. Solid-solution strengthening consists of two components, atomic-size and modulus mismatches [52], and their contributions pertaining to each element in the TTNZ alloys are shown in Fig. 8c and d. The Zr-content dependence of the modulus mismatch for all four elements shows the same trend as the Zr dependence of $\Delta \sigma_i$, while the Zr dependence of the atomic-size mismatch pertaining to all

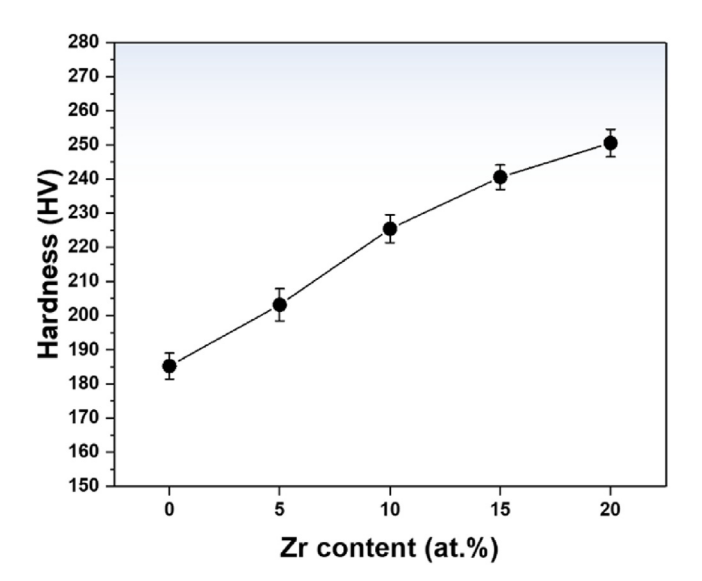


Fig. 9 - Experimental hardness of TTNZ alloys.

elements exhibits a monotonic-increase behavior, indicating that the contribution of the modulus mismatch is the dominant factor in the solid-solution strengthening. By comparing the values of $c_i |\delta_{G_i}|$ and $c_i |\alpha \delta_{r_i}|$, we further notice that the modulus mismatch contributions pertaining to the Ti, Ta, and Nb elements are higher than the effect of the atomic size mismatch but the atomic size and modulus mismatches pertaining to the Zr element have a comparable effect to solid-solution strengthening. The presented findings are contrary to the previous studies that lattice distortion is the dominant contribution to the solid-solution strengthening [9,22].

5. Conclusion

In summary, the present study fabricated single-phase BCC ${\rm Ti}_{65\text{-x}}{\rm Ta}_{25}{\rm Nb}_{10}{\rm Zr}_{\rm x}$ (x = 0, 5, 10, 15, and 20) refractory concentrated alloys. The microstructure of these alloys was examined by XRD, and SEM equipped with EBSD and EDS. The local distortion was studied based on DFT calculations. The influence of LLD on the mechanical properties was studied by a combination of DFT method and compression and hardness tests, respectively. The following conclusions can be achieved:

- 1) Contrary to slow grain growth behavior found in other RHEAs, the average grain size in TTNZ RHEAs increases monotonically with the increasing concentration of Zr after recrystallized at 1100 °C, proving a fast grain growth kinetics with the increase of Zr solute in the TTNZ RHEAs.
- 2) The increase of Zr concentration increases the LLD in TTNZ RHEAs, but the DFT calculations indicate LLD is overestimated by the conventional hard sphere model which ignores the chemical effects among constituent elements.
- 3) The yield strength and hardness of TTNZ RHEAs monotonously increases with increasing Zr. The quantitative solid-solution strengthening analysis demonstrates that the addition of Zr improves not only the atomic-size mismatch significantly but also the modulus mismatch dramatically. The modulus mismatch is the dominant factor for solid-solution strengthening rather than the atomic size mismatch.

Declaration of Competing Interest

The authors declare that they have no known competing financial interests or personal relationships that could have appeared to influence the work reported in this paper.

Acknowledgements

S. C. acknowledges the financial support from the National Natural Science Foundation of China (no. 52001271). Y. T. acknowledges the financial supports by Taishan Scholars Program of Shandong Province (tsqn202103052), and Top

Discipline in Materials Science of Shandong Province. F. M. appreciates the support from Natural Science Foundation of Shandong Province (ZR2021QE110). P. K. L. appreciates the support from the National Science Foundation (DMR-1611180 and 1809640) and the US Army Research Office (W911NF-13-1-0438 and W911NF-19-2-0049).

REFERENCES

- [1] Yeh JW, Chen SK, Lin SJ, Gan JY, Chin TS, Shun TT, et al. Adv Eng Mater 2004;6:299–303.
- [2] Cantor B, Chang ITH, Knight P, Vincent AJB. Mater Sci Eng 2004;375–377:213–8.
- [3] Zhang Y, Zuo TT, Tang Z, Gao MC, Dahmen KA, Liaw PK, et al. Prog Mater Sci 2014;61:1–93.
- [4] Łoński W, Spilka M, Kądziołka-Gaweł M, Gębara P, Radoń A, Warski T, et al. J Alloys Compd 2022;905:164074.
- [5] Ye YF, Wang Q, Lu J, Liu CT, Yang Y. Mater Today 2016;19:349–62.
- [6] Toda-Caraballo I, Wróbel J, Dudarev S, Nguyen-Manh D, Rivera-Díaz-del-Castillo PJAM. Acta Mater 2015;97:156–69.
- [7] Diao H, Santodonato LJ, Tang Z, Egami T, Liaw PK. JOM (J Occup Med) 2015;67:2321–5.
- [8] Guo W, Dmowski W, Noh J-Y, Rack P, Liaw PK, Egami T. Metall Mater Trans 2013;44:1994-7.
- [9] Lee C, Song G, Gao MC, Feng R, Chen P, Brechtl J, et al. Acta Mater 2018;160:158–72.
- [10] Babilas R, Łoński W, Boryło P, Kądziołka-Gaweł M, Gębara P, Radoń A. J Magn Magn Mater 2020;502:166492.
- [11] Tong Y, Velisa G, Zhao S, Guo W, Yang T, Jin K, et al. Materialia 2018;2:73–81.
- [12] Li L, Fang Q, Li J, Liu B, Liu Y, Liaw PK. Mater Sci Eng 2020;784:139323.
- [13] Senkov ON, Senkova SV, Miracle DB, Woodward C. Mater Sci Eng 2013;565:51–62.
- [14] Tong Y, Jin K, Bei H, Ko JYP, Pagan DC, Zhang Y, et al. Mater Des 2018;155:1-7.
- [15] Tong Y, Zhao S, Jin K, Bei H, Ko JYP, Zhang Y, et al. Scripta Mater 2018;156:14—8.
- [16] Ye YF, Zhang YH, He QF, Zhuang Y, Wang S, Shi SQ, et al. Acta Mater 2018:150:182–94.
- [17] Zhao YY, Nieh TG. Intermetallics 2017;86:45-50.
- [18] Kube SA, Sohn S, Uhl D, Datye A, Mehta A, Schroers J. Acta Mater 2019;166:677–86.
- [19] Tong Y, Zhao S, Bei H, Egami T, Zhang Y, Zhang F. Acta Mater 2020:183:172–81.
- [20] Samolyuk GD, Osetsky YN, Stocks GM, Morris JR. Phys Rev Lett 2021;126:025501.
- [21] Lee C, Chou Y, Kim G, Gao MC, An K, Brechtl J, et al. Adv Mater 2020;32(49):2004029.
- [22] Sohn SS, Kwiatkowski da Silva A, Ikeda Y, Kormann F, Lu W, Choi WS, et al. Adv Mater 2019;31(8):1807142.
- [23] Oh HS, Kim SJ, Odbadrakh K, Ryu WH, Yoon KN, Mu S, et al. Nat Commun 2019;10(1):2090.
- [24] Kresse G, Furthmüller J. Phys Rev B 1996;54:11169.
- [25] Vitos L. Computational quantum mechanics for materials engineers: the EMTO method and applications. London: Springer; 2007.
- [26] Zunger A, Wei S, Ferreira LG, Bernard JE. Phys Rev Lett 1990;65:353–6.
- [27] Ångqvist M, Muñoz WA, Rahm JM, Fransson E, Durniak C, Rozyczko P, et al. Adv. Theory Simul. 2019;2(7):1900015.
- [28] Wang H, Li M. Phys Rev B 2009;79:224102.
- [29] Toby BH. J Appl Crystallogr 2001;34:210-3.
- [30] Guo S, Liu CT. Prog Nat Sci: Mater Int 2011;21(6):433-46.

- [31] Zhang Y, Zhou YJ, Lin JP, Chen GL, Liaw PK. Adv Eng Mater 2008;10:534—8.
- [32] Meng F, Zhang W, Zhou Z, Sheng R, Chuang AC-P, Wu C, et al. Scripta Mater 2021;203:114104.
- [33] Wortman JJ, Evans RA. J Appl Phys 1965;36:153-6.
- [34] Brantley WA. J Appl Phys 1973;44:534-5.
- [35] Hill R. Proc Phys Soc 1952;65:349-54.
- [36] Feng X, Zhang K, Zheng Y, Zhou H, Wan Z. Nucl Instrum Methods Phys Res, Sect B 2019;457:56–62.
- [37] Mohammad-Ebrahimi M, Zarei-Hanzaki A, Abedi HR, Vakili SM, Soundararajan CK. J Alloys Compd 2021;874:159849.
- [38] Cao P, Huang H, Jiang S, Liu X, Wang H, Wu Y, et al. J Mater Sci Technol 2022;122:243–54.
- [39] Bai W, Tian Y, Xu G, Yang Z, Liu L, Masset PJ, et al. Calphad 2019;64:160-74.
- [40] Wang J, Fang L, Li X, Liu F, He X, Xu G, et al. J Alloys Compd 2022;910:164910.
- [41] Wang J, Fang L, Li X, Xu C, He X, Xu G, et al. Calphad 2022;77:102410.
- [42] Fan F, Gu Y, Xu G, Chang H, Cui Y. J Phase Equilibria Diffus 2019;40:686–96.

- [43] Liu Y, Pan T, Zhang L, Yu D, Ge Y. J Alloys Compd 2009;476:429–35.
- [44] Thirathipviwat P, Song G, Jayaraj J, Bednarcik J, Wendrock H, Gemming T, et al. J Alloys Compd 2019;790:266–73.
- [45] Senkov ON, Scott JM, Senkova SV, Miracle DB, Woodward CF. J Alloys Compd 2011;509:6043—8.
- [46] Juan C-C, Tsai M-H, Tsai C-W, Hsu W-L, Lin C-M, Chen S-K, et al. Mater Lett 2016;184:200—3.
- [47] Yao HW, Qiao JW, Hawk JA, Zhou HF, Chen MW, Gao MC. J Alloys Compd 2017;696:1139-50.
- [48] Yao H, Qiao J-W, Gao M, Hawk J, Ma S-G, Zhou H. Entropy 2016;18.
- [49] http://www.goodfellow.com/.
- [50] Martienssen W, Warlimont H. Springer handbook of condensed matter and materials data. Berlin, Heidelberg: Springer; 2006.
- [51] Senkov ON, Miracle DB, Chaput KJ, Couzinie J-P. J Mater Res 2018;33:3092—128.
- [52] Coury FG, Kaufman M, Clarke AJ. Acta Mater 2019;175:66-81.